Exp Eye Res. Author manuscript; available in PMC 2022 Jul 1.
Published in final edited form as:
Exp Eye Res. 2022 Jul; 220: 109102.
Published online 2022 May 5. doi: 10.1016/j.exer.2022.109102

PMCID: PMC9233048
NIHMSID: NIHMS1807075
PMID: 35525298

Engineering a 3D hydrogel system to study optic nerve head astrocyte morphology and behavior

Ana N. Strat,[a,b,c] Alexander Kirschner,[a] Hannah Yoo,[a] Ayushi Singh,[a,c,d] Tyler Bagué,[a] Haiyan Li,[a,c,d] Samuel Herberg,[a,c,d,e,f] and Preethi S. Ganapathy[a,b,c,*]

Abstract

In glaucoma, astrocytes within the optic nerve head (ONH) rearrange their actin cytoskeleton, while becoming reactive and upregulating intermediate filament glial fibrillary acidic protein (GFAP). Increased transforming growth factor beta 2 (TGF β2) levels have been implicated in glaucomatous ONH dysfunction. A key limitation of using conventional 2D culture to study ONH astrocyte behavior is the inability to faithfully replicate the *in vivo* ONH microenvironment. Here, we engineer a 3D ONH astrocyte hydrogel to better mimic *in vivo* mouse ONH astrocyte (MONHA) morphology, and test induction of MONHA reactivity using TGF β2. Primary MONHAs were isolated from C57BL/6J mice and cell purity confirmed. To engineer 3D cell-laden hydrogels, MONHAs were mixed with photoactive extracellular matrix components (collagen type I, hyaluronic acid) and crosslinked for 5 minutes using a photoinitiator (0.025% riboflavin) and UV light (405–500 nm, 10.3 mW/cm^2). MONHA-encapsulated hydrogels were cultured for 3 weeks, and then treated with TGF β2 (2.5, 5.0 or 10 ng/ml) for 7 days to assess for reactivity. Following encapsulation, MONHAs retained high cell viability in hydrogels and continued to proliferate over 4 weeks as determined by live/dead staining and MTS assays. Sholl analysis demonstrated that MONHAs within hydrogels developed increasing process complexity with increasing process length over time. Cell processes connected with neighboring cells, coinciding with Connexin43 expression within astrocytic processes. Treatment with TGF β2 induced reactivity in MONHA-encapsulated hydrogels as determined by altered F-actin cytoskeletal morphology, increased GFAP expression, and elevated fibronectin and collagen IV deposition. Our data sets the stage for future use of this 3D biomimetic ONH astrocyte-encapsulated hydrogel to investigate astrocyte behavior in response to injury.

Keywords: Reactive gliosis, Transforming growth factor beta 2, Extracellular matrix, GFAP, Fibronectin, Collagen IV, Glaucoma, Biomechanical Strain

1. Introduction

Glaucoma is a chronic progressive optic neuropathy that leads to irreversible blindness due to the loss of retinal ganglion cells (RGCs) (Neumann et al., 2014; Weinreb et al., 2014). The main risk factor for the disease is elevated intraocular pressure (IOP). As such, current medical and surgical interventions are designed to lower IOP to prevent disease progression (Stein et al., 2021; Weinreb et al., 2014). However, much of the mechanism of how IOP affects RGC viability remains unknown. RGCs are initially damaged within the optic nerve head (ONH) (Crawford Downs et al., 2011; Neumann et al., 2014; Weinreb et al., 2014), which contains lamina cribrosa cells, astrocytes, microglia, and an extracellular matrix (ECM) network that supports RGC axons as they leave the globe through the optic nerve (Hernandez et al., 1986, 1988). IOP elevation in glaucoma strongly correlates with aberrant ONH ECM remodeling and increased mechanical stress on RGC axons. Of the cells within the ONH, astrocytes are compelling candidates for transducing IOP insult into changes in ECM structure. Moreover, ONH astrocytes have been identified as key modulators of RGC axonal health in both early and late stages of disease (Clarke et al., 2018; Cooper et al., 2018).

Early in glaucoma, it is likely that astrocytes are protective to RGCs (Cooper et al., 2020; Sun et al., 2017). Immediately after IOP elevation in rodents, astrocytes within the ONH become reactive and upregulate intermediate filament glial fibrillary acidic protein (GFAP) levels (Cooper et al., 2020). Astrocytes additionally rearrange their actin cytoskeleton and cellular processes, coinciding with Connexin 43 (CX43) gap-junction coupling, to promote axonal health (Cooper et al., 2018, 2020; Sun et al., 2017; Tehrani et al., 2016, 2019). However, later in the disease process in rodent glaucoma models, there is evidence that excessive astrocytic reactivity is neurotoxic to RGCs (Liddelow et al., 2017; Sloan and Barres, 2014; Sterling et al., 2020). Reactive astrocytes secrete both ECM crosslinking and degrading enzymes and upregulate pro-fibrotic cytokines such as transforming growth factor beta 2 (TGFβ2), which can significantly impact ECM integrity (Hernandez, 2000). Many studies implicate a role of elevated TGFβ2 in ECM remodeling within the glaucomatous ONH (Kim et al., 2017; Pena et al., 1999; Zode et al., 2011). Thus, careful investigation of the relationship between glaucomatous insults (such as IOP-induced strains and TGFβ2), ONH astrocyte behavior, and the surrounding ECM (i.e., stiffness and composition) is integral to understanding glaucoma pathobiology. Our overarching goal is to develop a model system ideal for investigating this relationship.

Monolayer ONH astrocyte cultures subjected to biochemical (i.e., TGFβ2 treatment) or mechanical (i.e., hydrostatic pressure) stressors frequently display increased reactivity, actin remodeling, and upregulation of ECM protein production (Ricard et al., 2000). However, there are significant limitations to studying glaucoma pathophysiology using 2D monolayer cultures. Astrocytes, when cultured on supra-physiologically stiff substrates such as glass or plastic (Caliari and Burdick, 2016) display a reactive phenotype and lack their characteristic stellate morphology. Additionally, they fail to form a typical star shape in 2D (Hernandez, 2000). In an attempt to better mimic *in vivo* astrocyte stellate morphology and to limit baseline reactivity, a few groups have used viscoelastic hydrogel systems (i.e., water-swollen networks of natural or synthetic polymers) to provide more biologically relevant substrates for cell growth (Mulvihill et al., 2018; Placone et al., 2015). Few preliminary studies have described rat optic nerve head astrocyte-encapsulated hydrogels (Boazak et al., 2019; Foltz et al., 2021). Our work seeks to further the existing literature by encapsulating

mouse ONH astrocytes inside a 3D polymer network, systematically characterizing time-dependent process complexity, and analyzing cellular reactivity in response to a known inducer of astrocyte reactivity.

We recently described a novel tissue-engineered 3D trabecular meshwork hydrogel system (Li et al., 2021) by mixing human trabecular meshwork cells with ECM biopolymers (collagen type I, hyaluronic acid; HA, and elastin-like polypeptide) followed by photoinitiator-mediated short UV crosslinking. Building on this previous work, in the present study we engineer a hydrogel-based model system containing mouse ONH astrocytes (MONHAs) and photoactive ECM proteins (collagen type I and HA) that is crosslinked with UV light using 0.025% riboflavin as photoinitiator to (1) better mimic ONH astrocyte stellate morphology and cell-cell interactions, and (2) reliably induce ONH astrocyte reactivity and ECM production in response to a known stressor. Focusing on astrocyte morphology, we characterized length and complexity of cellular processes over time using Sholl analysis. We investigated whether MONHAs retain astrocyte markers GFAP and CX43 expression after four weeks in culture. Lastly, to test whether encapsulated MONHAs can become reactive, cell-laden hydrogels were treated with TGFβ2 followed by assessment of GFAP expression, actin cytoskeletal remodeling, and ECM protein deposition in 3D.

2. Methods

2.1. MONHA isolation and culture

C57BL/6J mice were purchased from the Jackson Laboratory (Bar Harbor, ME) and bred in house according to the institutional guidelines for the humane treatment of animals (IACUC #473) and to the ARVO Statement for the Use of Animals in Ophthalmic and Vision Research. For each harvest in this study 6–8 mice aged 6–8 weeks were used. The isolation of primary MONHAs and cell culture was performed as previously described (Kirschner et al., 2021). Briefly, using a SMZ1270 stereomicroscope (Nikon Instruments, Melville, NY), ONH tissue was dissected from each ocular globe proximal to the sclera. Tissue samples were digested in 0.25% trypsin (Invitrogen, 25200–056, Carlsbad, CA) for 15 min at 37 °C and then resuspended in MONHA growth medium (Dulbecco's modified Eagle's medium, DMEM/F12 (Invitrogen, 11330–032) + 10% fetal bovine serum (Atlanta Biologicals, S11550, Atlanta, GA) + 1% penicillin/streptomycin (Corning, 30-001-CI, Manassas, VA) + 1% Glutamax (Invitrogen, 35050–061, Grand Island, NY) + 25 ng/ml epidermal growth factor (EGF; Sigma, E4127–5X, St. Louis, MO). After digestion ONH tissue was plated on 0.2% gelatin (Sigma, G1393) coated T75 cell culture flasks and kept at 37 °C in a humidified atmosphere with 5% CO_2. MONHAs migrated from ONH tissue over 10–14 days before first passage. Eight separate MONHA isolations (04–11) were used for all experiments in this manuscript.

2.2. MONHA cell characterization

MONHAs were seeded at 1×10^4 cells/cm^2 on sterile glass coverslips in 24-well culture plates (Thermo Fisher Scientific, Waltham, MA). After 48 h, cells were fixed with 4% paraformaldehyde (PFA; J19943-K2, Thermo Fisher Scientific) at room temperature for 10 min, and permeabilized with 0.5% Triton X-100 (Thermo Fisher Scientific, 85111) at room temperature for 30 min. Cells

were washed in Dulbecco's Phosphate Buffered Saline 1X (DPBS; Invitrogen, 14190–44) and blocked (PowerBlock; Biogenx, HK085–5K, San Ramon, CA) for 1 h at room temperature. Cells were then incubated for 1 h at room temperature with rabbit anti-glial fibrillary acidic protein (GFAP; rabbit anti-GFAP antibody, 1:300, Dako, Z0334, Carpinteria, CA), rabbit anti-water channel aquaporin 4 (AQP4; rabbit anti-AQP4 antibody, 1:300, Sigma, A5971), rabbit anti-oligodendrocyte specific protein (OSP; rabbit anti-OSP antibody, 1:100, Abcam, Ab53041, Cambridge, MA) or rat anti-F4/80 (rat anti-F4/80 antibody, 1:50, BioRad, MCA497GA, Hercules, CA). Cells were again washed in DPBS and incubated for 1 h at room temperature with Alexa Fluor® 488-conjugated secondary antibody (goat polyclonal antibody to rabbit IgG, 1:500, Abcam, Ab15077). Nuclei were counterstained with 4′,6′-diamidino-2-phenyliondole (DAPI; Invitrogen, D1306). Coverslips were mounted with ProLong™ Gold Antifade (Thermo Fisher Scientific, P36930) on Superfrost™ Plus microscope slides (Fisher Scientific) and fluorescent images were acquired with Eclipse N*i* microscope (Nikon). Four fields of view at 20× magnification were taken from each coverslip per culture. Number of GFAP-, OSP-, or F4/80-positive cells versus total number of cells were quantified from acquired images. In conjunction, SYBR™ Green based quantitative real-time polymerase chain reaction (qRT-PCR) was performed on RNA extracted from primary MONHA using PureLink RNA Mini Kit (Invitrogen). A NanoDrop spectrophotometer (Thermo Fisher Scientific) was used to confirm RNA concentrations, and RNA samples were then reverse transcribed using iScript cDNA Synthesis Kit (BioRad, Hercules, CA, USA). cDNA (100 ng) was amplified in triplicates in each 40-cycle reaction using a CFX 384 Real Time PCR System (BioRad) with an annealing temperature of 60 °C, Power SYBR™ Green PCR Master Mix (Thermo Fisher Scientific), and custom-designed qRT-PCR primers (Table 1). The mRNA transcript levels were normalized to endogenous control 18s rRNA, and relative mRNA expression levels calculated according to the comparative C_T method (Schmittgen and Livak, 2008).

Table 1

Primer sequences used for qRT- PCR in mouse primary ONH astrocytes.

Name	Forward primer (5′ → 3′)	Reverse primer (5′ → 3′)
18s rRNA	AGGATGTGAAGGATGGGAAG	TTCTTCAGCCTCTCCAGGTC
GFAP	AGAAAGGTTGAATCGCTGGA	CGGCGATAGTCGTTAGCTTC
Nestin	CCCTGAAGTCGAGGAGCTG	CTGCTGCACCTCTAAGCGA
Vimentin	GCTATGTGACCACGTCCACA	GTCCACCGAGTCTTGAAGCA
AQP4	CTGGGCATCCTGTCACAACA	CAGGAATGTCCACACTTAGACAC
AQP4	CCCGCAGTTATCATGGGAAA	CCACATCAGGACAGAAGACATAC
CX43	GAACACGGCAAGGTGAAGAT	GAGCGAGAGACACCAAGGAC

2.3. Astrocyte migration by scratch - wound assay

MONHAs were seeded at 1.5 × 10^4 cells/cm^2 per well in a 24-well culture plate (Thermo Fisher Scientific, Waltham, MA). After 24 h, the bottom of each well was scratched using a 1000-µL pipet tip vertically across the middle of the well. Immediately after scratch wound, brightfield images of each well were taken to establish the scratch width at time 0. The astrocytes were then kept in culture for 24 h. Brightfield images of each scratch width per well were captured at 3 h, 6 h, 12 h, and 24 h. Using Fiji software (NIH, Bethesda, MD), the area of scratch per well was obtained and subsequently, the wound width was determined at time 0 and over time. The astrocytes depicted within the initial wound width at different time points were characterized as migrating cells.

2.4. Hydrogel precursor solutions

Methacrylate-conjugated bovine collagen type I (MA-COL; molecular weight: ~300 kDa, degree of methacrylation: ~60–70%; Advanced BioMatrix, Carlsbad, CA, USA) was reconstituted according to the manufacturer's instructions with sterile 20 mM acetic acid at 4 mg/ml; 1 ml MA-COL was neutralized with 90 µl neutralization buffer (Advanced BioMatrix) for hydrogel use. Thiol-conjugated hyaluronic acid (SH-HA; Glycosil®; molecular weight: ~300 kDa, degree of thiolation: ~20–30%; Advanced BioMatrix) was reconstituted in sterile diH2O at 10 mg/ml according to the manufacturer's instructions.

2.5. Preparation of PDMS molds

A 10:1 ratio of elastomer to curing agent was prepared according to the manufacturer's protocol for polydimethylsiloxane (PDMS; Sylgard 184, Dow Corning, Midland, MI, USA). Using a 3D printer (F170; Stratasys, Eden Prairie, MN, USA), 10 mm diameter × 1 mm depth negative molds were made from ABS-M30 filament. The PDMS mixture was poured into the negative molds and degassed in a desiccator under vacuum before curing overnight at 60 °C. PDMS molds were sterilized prior to use in culture.

2.6. Preparation of MONHA-encapsulated hydrogels

MONHAs (2.5 × 10^6 cells/ml or 5.0 × 10^6 cells/ml) in media were mixed with 3.1 mg/ml methacrylate-conjugated bovine collagen type I, 1 mg/ml thiol-conjugated hyaluronic acid, and 0.025% (w/v) riboflavin (Sigma, R7774) (photoinitiator) on ice (Fig. 1). The chilled MONHA hydrogel precursor solution was pipetted as (1) 10 µl droplets onto PDMS-coated (Sylgard 184; Dow Corning) 24-well culture plates, (2) 30 µl droplets onto 12 mm round glass coverslips sandwiched with Surfasil (Fisher Scientific) coated coverslips on top, or 80 µl into custom 10 × 1 mm PDMS molds. Constructs were then crosslinked by exposure to UV light (OmniCure S1500 UV Spot Curing System; Excelitas Technologies, Mississauga, Ontario, Canada) at 405–500 nm, 10.3 mW/cm^2 for 5 min. MONHA growth medium was added to each well and replenished every 2–3 days, and constructs were cultured for 1–4 weeks.

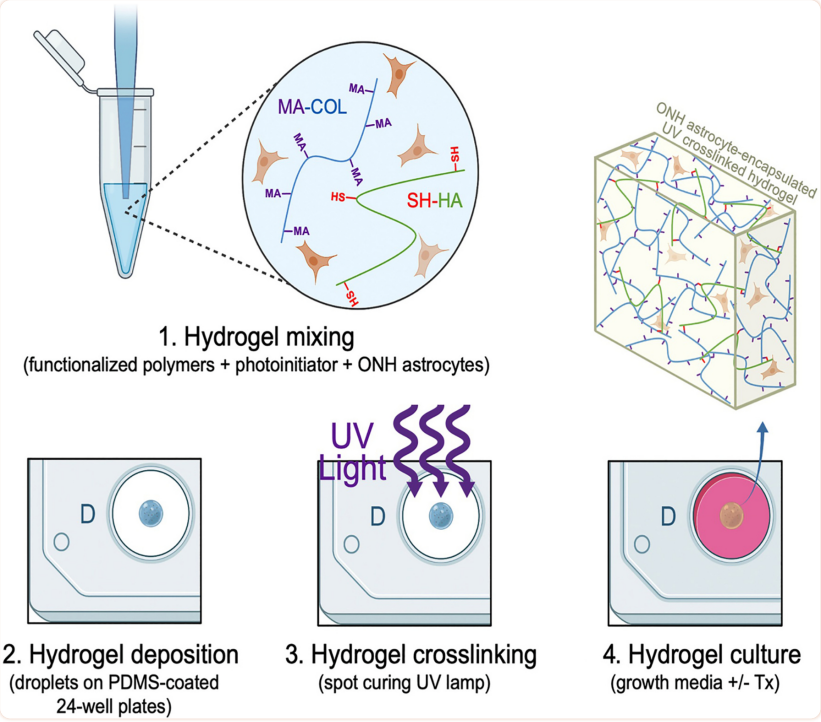

Fig. 1.

Schematic of MONHA-encapsulated hydrogel formulation.

2.7. MONHA hydrogel rheology analysis

Acellular and MONHA-encapsulated hydrogels were created using 80 μl of hydrogel mixture per 10 × 1 mm PDMS mold. Samples were UV crosslinked as described in Methods 2.6. Hydrogel viscoelasticity of acellular and MONHA-encapsulated hydrogels (N = 4 per group) was obtained at day 0 using a Kinexus rheometer (Malvern Panalytical, Westborough, MA, USA) fitted with an 8 mm diameter parallel plate. Rheometry measures were performed similarly to Li et al. (2021). Briefly, the 8 mm geometry was lowered on top of the hydrogels to a calibration normal force of 0.02 N, and an oscillatory shear-strain sweep test (0.1–60%, 1.0 Hz, 25 °C) determined values for storage modulus (G′) and loss modulus (G′′) in the linear region. Storage modulus for each sample was then converted to elastic modulus (E) calculated as E = 2 * (1 + v) * G′, with Poisson's ratio (v) of 0.5 assumed for the ECM hydrogels (Li et al., 2022; Lodge and Hiemenz, 2020).

2.8. MONHA-encapsulated hydrogel cell viability and proliferation analysis

Using a LIVE/DEAD™ Viability/Cytotoxicity Kit (i.e., live = green-stained, dead = red-stained) (Invitrogen), cell viability was assessed. MONHA hydrogels were incubated at 37 °C for 45 min with the staining solutions (calcein-AM (0.5 μl/ml) and ethidium homodimer-1 (2 μl/ml)) diluted in media according to the manufacturer's instructions and then washed with DPBS. Fluorescent images were captured after initial UV crosslinking on day 0 (N = 3 per group), and weeks 1–4 with

an Eclipse *Ti* microscope (Nikon). Four quadrants per hydrogel were imaged and analyzed on day 0 to quantify percent MONHA cell viability (i.e., ratio of live to total cells). Cell proliferation was quantified with the CellTiter 96® Aqueous Non-Radioactive Cell Proliferation Assay (Promega, Madison, WI, USA) as per manufacturer's instructions. MONHA-encapsulated hydrogels were incubated with the staining solution (38 µl MTS, 2 µl PMS solution, 200 µl media) at 37 °C for 90 min. Absorbance at 490 nm was then assessed with a spectrophotometer plate reader (BioTEK, Winooski, VT, USA). Fold-change over time of blank-corrected absorbance values was analyzed to quantify cell proliferation in hydrogels.

2.9. MONHA-encapsulated hydrogel cell morphology and immunocytochemistry analysis

MONHA-encapsulated hydrogels on glass coverslips were fixed with 4% PFA at 4 °C overnight, permeabilized with 0.5% Triton™ X-100 (Thermo Fisher Scientific), blocked with blocking buffer (BioGeneX), and stained for filamentous F-actin, GFAP, or CX43 as previously described (Li et al., 2021; Kirschner et al., 2021). Briefly, MONHA-encapsulated hydrogels were stained for F-actin with Alexa fluor® 488- or 594- conjugated Phalloidin (1:500, Abcam, Ab176757 or Ab176753) and primary antibody against GFAP (rabbit anti-GFAP, 1:100, Dako, Z0334) or CX43 (rabbit anti-CX43, 1:100, Cell Signaling Technologies, 3512) overnight, followed by incubation with an Alexa Fluor® 488-conjugated secondary antibody (goat polyclonal antibody to rabbit IgG, 1:500, Abcam, Ab150077). Nuclei were counterstained with DAPI, and fluorescent images were acquired using an Eclipse N*i* microscope (Nikon).

2.10. Confocal microscopy and 3D analysis

Phalloidin-stained images of MONHA-encapsulated hydrogels were captured using Zeiss LSM510 scanning confocal microscope. The image size was set to 1024 × 1024 pixels in x/y with a resolution of 0.42 µm per pixel. Individual z-stacks consisted of 5 slices with the z-step interval set to 1.5 µm. The analysis for signal intensity was determined using Z-project Maximum Intensity Projection in Fiji (NIH) across individual z-stacks.

2.11. MONHA-encapsulated hydrogel cell morphology analysis

Phalloidin-stained confocal z-stack images were analyzed in Fiji. Tracings of cell processes and branching were performed using Fiji plugin NeuronJ. Sholl analysis was conducted to evaluate process complexity, i.e., the number of astrocytic processes intersecting concentric spheres originating from the cell body (Lye-Barthel et al., 2013). Total mean process length (mean of total processes + branches) and degree of branching (number of primary processes and branches/number of primary processes) were analyzed for each cell (Placone et al., 2015).

2.12. MONHA-encapsulated hydrogel treatments and analysis of F-actin levels

MONHA-encapsulated hydrogels were cultured in MONHA growth medium for 21 days followed by treatment with increasing doses of TGFβ2 (vehicle control, 2.5 ng/ml, 5 ng/ml, and 10 ng/ml; R&D Systems, Minneapolis, MN) for 7 days. Hydrogels were subsequently stained with Alexa

fluor® 488- or 594-conjugated Phalloidin and confocal imaging acquired as described in Methods 2.10. Fold changes in normalized F-actin expression were analyzed from quantification over four fields of view per coverslip with background subtraction.

2.13. MONHA-encapsulated hydrogel sectioning and immunohistochemical analysis

MONHA-encapsulated hydrogels cultured for 21 days were treated with TGFβ2 for 7 days before 4% PFA fixation at 4 °C overnight. Subsequently, hydrogels were incubated in 30% sucrose at 4 °C for an additional 24 h. They were then washed with DPBS and embedded in Tissue-Plus™ O.C.T. Compound (Fisher Scientific) before flash freezing in liquid nitrogen. Using a cryostat (Leica Biosystems Inc., Buffalo Grove, IL, USA) 20 μm sections were cut and collected on Superfrost™ Plus microscope slides (Fisher Scientific). Cellular hydrogel sections were permeabilized with 0.5% Triton™ X-100, incubated in blocking buffer for 1 h, and then immunostained for either fibronectin (rabbit anti-fibronectin antibody, 1:500, Abcam, Ab45688), collagen IV (rabbit anti-collagen IV antibody, 1:500; Abcam, Ab6586), or GFAP (rabbit anti-GFAP antibody, 1:100, Dako) overnight. Sections were then stained with Alexa Fluor® 488-conjugated secondary antibody (goat polyclonal antibody to rabbit IgG, 1:500, Abcam, Ab150077) for 1 h; nuclei were counterstained with DAPI. Slides were mounted with ProLong™ Gold Antifade (Thermo Fisher Scientific), and fluorescent images were acquired using an Eclipse N*i* microscope (Nikon) or Zeiss LSM510 scanning confocal microscope. Fold changes in normalized signal intensity were analyzed from quantification over three fields of view per section with background subtraction using FIJI (NIH, Bethesda, MD), as described in Methods 2.12.

2.14. Statistical analysis

Individual sample sizes are specified in each figure caption. Comparisons between groups were assessed by unpaired *t*-test, one-way, two-way, or main effect analysis of variance (ANOVA) with Tukey's multiple comparisons *post hoc* as appropriate. A two-way ANOVA main effect only model was used to analyze process complexity over time (i.e., 28 d) (Alexander et al., 2016). All data are shown with mean ± SD. The level of significance was set to $p < 0.05$ or lower. GraphPad Prism software v9.2 (GraphPad Software, La Jolla, CA, USA) was used for all analyses.

3. Results

3.1. MONHA-encapsulated hydrogel stiffness is within the range of neurological tissues

ONH astrocytes are a unique group of astrocytes, specifically residing within the unmyelinated portion of the optic nerve (Choi et al., 2015; Kimball et al., 2021). Primary astrocytes were isolated and cultured from ONH tissue from 6 to 8 weeks old C57BL/6J mice, and cell purity was confirmed as previously described (Suppl. Fig. 1A and B) (Kirschner et al., 2021). Cells were immunoreactive for the astrocyte marker GFAP, and negative for oligodendrocyte marker OSP and microglial/macrophage marker F4/80. ONH astrocytes, in contrast to astrocytes within the myelinated portion of the nerve, do not express aquaporin 4 (AQP4) (Kimball et al., 2021). Thus, we tested immunoreactivity for AQP4, which was negative. Morphologically, few cells appeared stel-

late in nature, but the majority of cultured astrocytes possessed large and polygonal cell bodies (Suppl. Fig. 1D). By qPCR analysis, cells expressed astrocyte markers GFAP, nestin, vimentin, and CX43 (Suppl. Fig. 1E). Using two different primer pairs (Table 1), AQP4 was undetectable in our cells (Suppl. Fig. 1E). Cultured cells retained migratory function, as is typical for astrocytes *in vivo* (Suppl. Fig. 1F and G). Thusly characterized MONHAs were used for all subsequent hydrogel experiments.

Astrocytes are abundantly present within the ONH, and they form a glial lamina occupying roughly half of the lamina cribrosa volume (Sun et al., 2009; Vecino et al., 2016). To determine optimal density of astrocytes to encourage stellate morphology and cell-cell interaction, we encapsulated 2.5×10^6 cells/ml and, separately, 5×10^6 cells/ml within our hydrogels. The tissue stiffness within central nervous system and ONH tissues range from 0.1 to 1.4 kPa (Budday et al., 2015, 2017). Previous astrocyte-encapsulated viscoelastic hydrogels have reported stiffnesses ranging from 0.0423 to 0.991 kPa (Hu et al., 2021). To determine the stiffness of our hydrogel system, we performed rheology measures on both acellular and MONHA-encapsulated hydrogels. Immediately after UV crosslinking, acellular hydrogels had an elastic modulus of 0.201–0.319 kPa, while 2.5×10^6 cells/ml MONHA-encapsulated hydrogels had an elastic modulus range of 0.310–0.368 kPa (Fig. 2A). Thus, MONHA-encapsulated hydrogels harbored stiffnesses within the physiologic range of neurologic and ONH tissues.

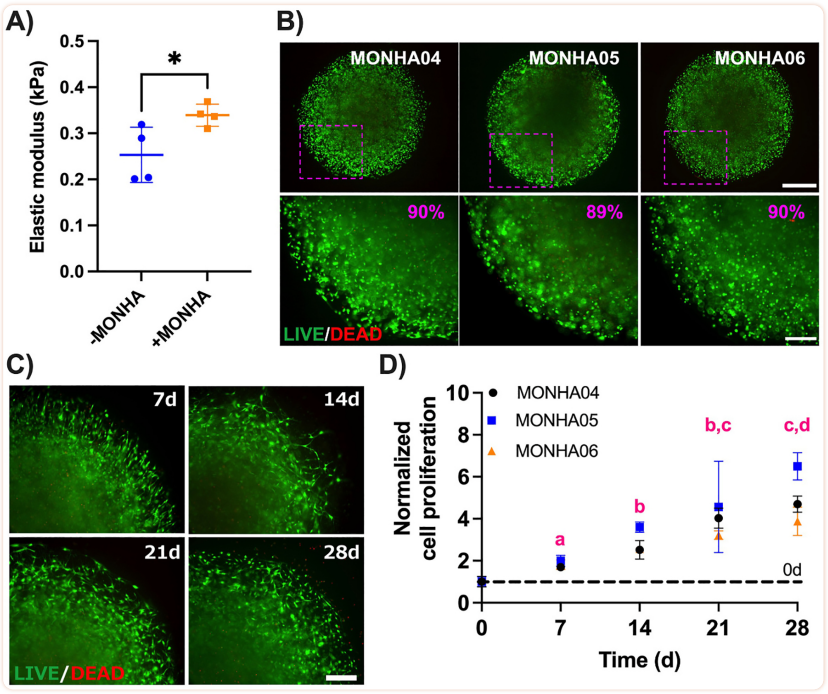

Fig. 2.

MONHA-encapsulated hydrogel stiffness, viability, and proliferation. (A) Elastic modulus of acellular and MONHA-encapsulated hydrogels (N = 4/group, *p = 0.0374). (B) Representative Live (green)/Dead (red) fluorescence images from 3 independent MONHA isolations immediately after crosslinking (N = 3/group). Pink percentage values depict average % live cells per hydrogel. Scale bars: 500 μm (top), 250 μm (bottom). (C) Longitudinal Live (green)/Dead (red) fluorescence images of representative hydrogels. Scale bar 250 μm. (D) Normalized cell proliferation over time (7 d, 14 d, 21 d, and 28 d; shared significance indicator letters represent nonsignificant difference ($p > 0.05$), distinct letters represent significant difference ($p < 0.05$)). Significance was determined by unpaired *t*-test (A) and two-way ANOVA using multiple comparisons tests (D) (*$p < 0.05$).

3.2. Astrocytes retain cell viability and proliferation over time

Immediately after UV crosslinking of MOHNA-encapsulated hydrogels (2.5×10^6 cells/ml), we measured astrocyte viability. Fig. 2B shows representative images of Live/Dead stained hydrogels from 3 independent MONHA isolations. Cellular viability after crosslinking was reproducibly >89% across isolations. Cell viability was maintained over 4 weeks (Fig. 2C) and cells continued to significantly proliferate in a near linear fashion during that time ($R^2 = 0.94$, 0.83, and 0.93 respectively) (Fig. 2D). We additionally encapsulated 5×10^6 cells/ml within our hydrogels and similarly found high cell viability immediately after crosslinking (Suppl. Fig. 2A). Interestingly, cellular proliferation at this density was not significantly increased over time (Suppl. Fig. 2B), indicating that a higher baseline density may limit continued cell proliferation within the construct. F-actin staining similarly demonstrated a high density of cellular processes (Suppl. Fig. 2C).

3.3. Astrocytes develop typical stellate morphology over time in the hydrogel system

Astrocyte morphology is typically stellate in nature with small cell bodies and radial primary processes and branches connecting to other astrocytes via gap junctions (Cooper et al., 2018; Oberheim et al., 2009; Sun et al., 2017). Astrocytes in our hydrogel system qualitatively demonstrated stellate morphology and extended processes and branches over time to promote interaction with neighboring astrocytes (Fig. 3A). This morphologic appearance in 3D is in stark contrast to the large polygonal cell bodies and short processes of MONHAs cultured in 2D on a glass substrate (Suppl. Fig. 3). Furthermore, after 4 weeks in 3D culture, MONHAs continued to express GFAP and CX43 (Fig. 3B,C), and thus, retained astrocyte-specific markers.

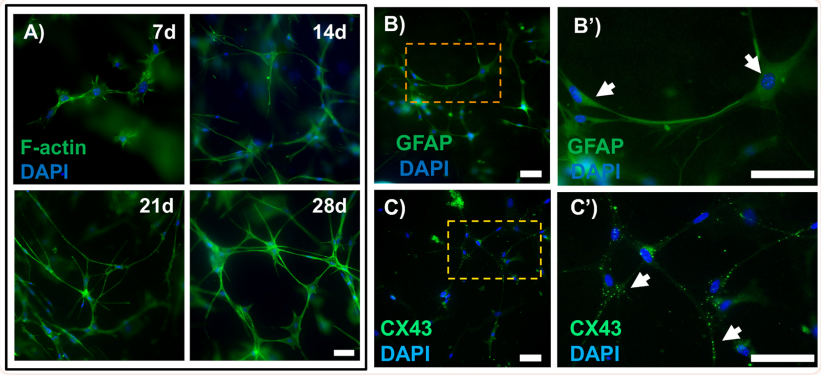

Fig. 3.

MONHA stellate morphology and astrocytic marker expression in hydrogels. (A) Representative fluorescence images of astrocyte morphology within hydrogels at 7 d, 14 d, 21 d, and 28 d. Scale bar: 100 μm. (B) Representative fluorescence images of astrocytes expressing GFAP (green) and (C) CX43 (green) in hydrogels at 28d. Scale bar: 100 μm. (B′-C′) Magnified images from boxed regions (orange) showing astrocytes expressing either GFAP (upper right, white arrows) or CX43 puncta (lower right, white arrows). Scale bar: 100 μm.

Confocal imaging of F-actin staining of individual cells within MONHA-encapsulated hydrogels were analyzed and illustrated process elongation over the course of three weeks (Fig. 4A–C). At 4 weeks, the rate of cell proliferation precluded analysis of distinct cells. Sholl analysis confirmed that increased time in culture significantly increased the length of astrocyte processes from 22.89 ± 2.693 μm at week 1, to 52.65 ± 3.034 μm at week 2 and 87.08 ± 5.214 μm at week 3 ($p < 0.0001$) (Fig. 4D). In contrast, the degree of branching reflective of the number of total primary processes divided by the number of total branches per cell, remained unchanged over time, which is consistent with reports of cortical astrocyte-encapsulated hydrogels (Fig. 4E) (Butt et al., 1994; Placone et al., 2015). The two-way ANOVA analysis revealed significant main and interaction effects for the length of culture time and number of process intersections (i.e., complexity) away from center of cell body. In general, the effect of increased time in culture for 14 d and 21 d MONHA-encapsulated hydrogels was most prominently significant ($p < 0.0001$), with number of process intersections away from center of cell body demonstrating increased complexity as well ($p < 0.05$), in comparison to 7 d MONHA-encapsulated hydrogels. Therefore, systematic analysis of MONHA process complexity revealed enhanced complexity after 2–3 weeks in culture as compared to week 1 following encapsulation (Fig. 4F).

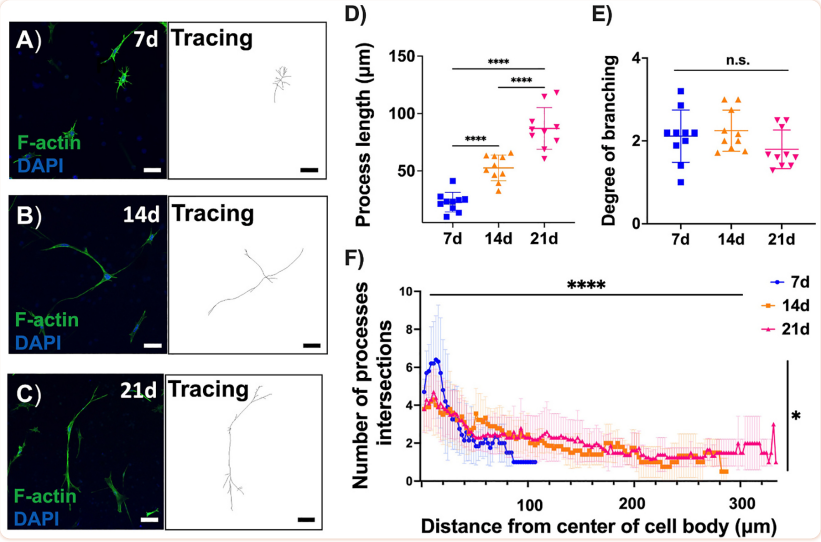

Fig. 4.

MONHA process length and branching in hydrogels. (A–C) F-actin staining and tracing of astrocytic morphology over time. Scale bar: 100 μm (A–B), 50 μm (C). (D–E) Process length and degree of branching of astrocytes. (F) Sholl analysis indicating the number of process intersections at each increasing radius from cell body for 7d, 14d, and 21d (N = 10 cells/group). Statistical significance was determined using one-way ANOVA (****$p < 0.0001$) for process length (D) and degree of branching (E), and two-way ANOVA main effects only model for process complexity over time (F) (main effect of time $F(149, 2012) = 8.778$, ****$p < 0.0001$, and main effect of process complexity $F(2, 2012) = 3.992$, *$p < 0.05$).

Taken together, these data support that 2–3 weeks culture within a 3D ECM facilitates development of increased MONHA process length/complexity. MONHA-encapsulated hydrogels cultured for 3 weeks were used in all subsequent experiments.

3.4. TGFβ2 induces GFAP expression, actin cytoskeletal rearrangement, and ECM deposition in MONHA-encapsulated hydrogels

In glaucoma, astrocytes within the ONH become reactive and undergo remodeling of their F-actin cytoskeleton (Sun et al., 2017; Tehrani et al., 2016). Elevated TGFβ2 levels have been demonstrated within the glaucomatous ONH; likewise, TGFβ2 induces astrocyte reactivity in 2D culture (Hernandez, 2000; Pena et al., 1999; Prendes et al., 2013; Wang et al., 2017a). Therefore, we asked whether exogenous TGFβ2 would induce astrocyte reactivity in our hydrogel system; to do so, we analyzed F-actin cytoskeletal levels, ECM protein deposition, and GFAP immunoreactivity.

MONHA-encapsulated hydrogels were cultured for 3 weeks prior to TGFβ2 treatment for 7 days (Suppl. Fig. 4A). Astrocytes retained viability and continued to proliferate across all groups (Suppl. Fig. 4B and C). MONHA-encapsulated hydrogels treated with TGFβ2 showed significant remodeling of F-actin networks (Fig. 5A) in a dose-dependent manner; an up to ~ 6-fold increase in F-actin

signal intensity compared to vehicle control-treated MONHA-encapsulated hydrogels was observed (Fig. 5B). Given the robust increase in F-actin intensity, treatment with 5 ng/ml TGFβ2 for 7 days was used for all subsequent experiments.

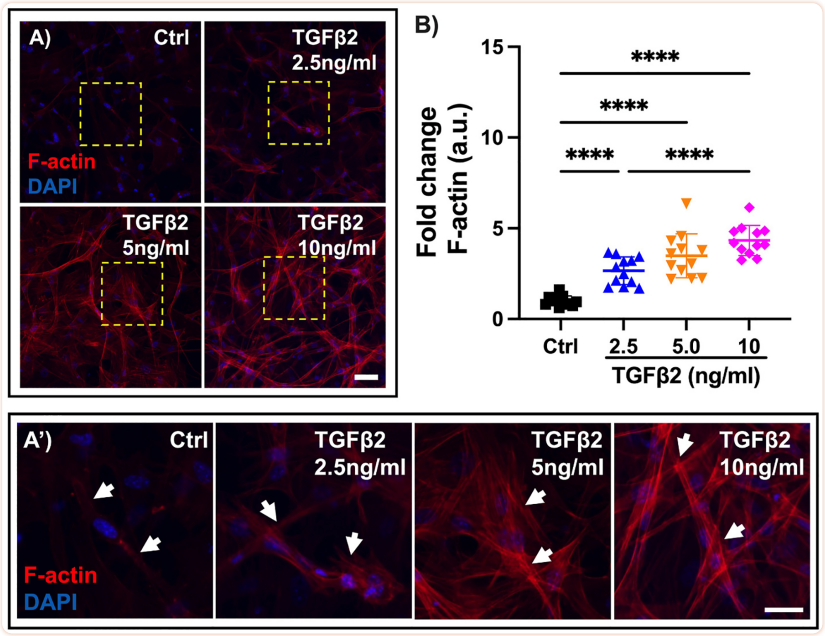

Fig. 5.

TGFβ2 effect on F-actin network in MONHA-encapsulated hydrogels. (A) Representative confocal fluorescence images of F-actin expression levels in control versus TGFβ2-treated MONHA-encapsulated hydrogels (2.5 ng/ml, 5 ng/ml, 10 ng/ml). Scale bar: 100 μm. (A′) Magnified images from boxed regions (yellow) of F-actin cytoskeletal changes (white arrows) in control versus TGFβ2-treated MONHA-encapsulated hydrogels (2.5 ng/ml, 5 ng/ml, 10 ng/ml). Scale bar: 50 μm. (B) Quantification of fold change in F-actin intensity (N = 10 fields of view/group). Statistical significance was determined using one-way ANOVA (****$p < 0.0001$) for F-actin expression levels (B).

Reactive astrocytes upregulate ECM proteins and intermediate filament protein GFAP (Hernandez, 2000), and elevated TGFβ2 levels are associated with ECM remodeling within the glaucomatous ONH (Kim et al., 2017; Zode et al., 2011). We previously showed that MONHAs in conventional 2D culture increased GFAP expression and ECM deposition in response to TGFβ2 treatment (Kirschner et al., 2021). Therefore, we asked whether exposure of MONHA-encapsulated constructs to 5 ng/ml TGFβ2 for 7 days would induce similar cellular responses in 3D culture.

Vehicle control treated MONHA-encapsulated hydrogels showed low baseline levels of collagen IV and fibronectin deposition, and GFAP expression (Fig. 6A, B, C). In contrast, TGFβ2-treatment induced a significant ~2.5-fold increase in collagen IV ($p < 0.0001$) and fibronectin ($p < 0.001$) signal (Fig. 6D and E). GFAP immunoreactivity increased ~7.4-fold compared to controls ($p < 0.0001$) (Fig. 6F). Taken together, these data indicate that MONHAs encapsulated within our ECM hydrogel respond reliably to a known inducer of astrocyte reactivity (i. e., exogenous TGFβ2).

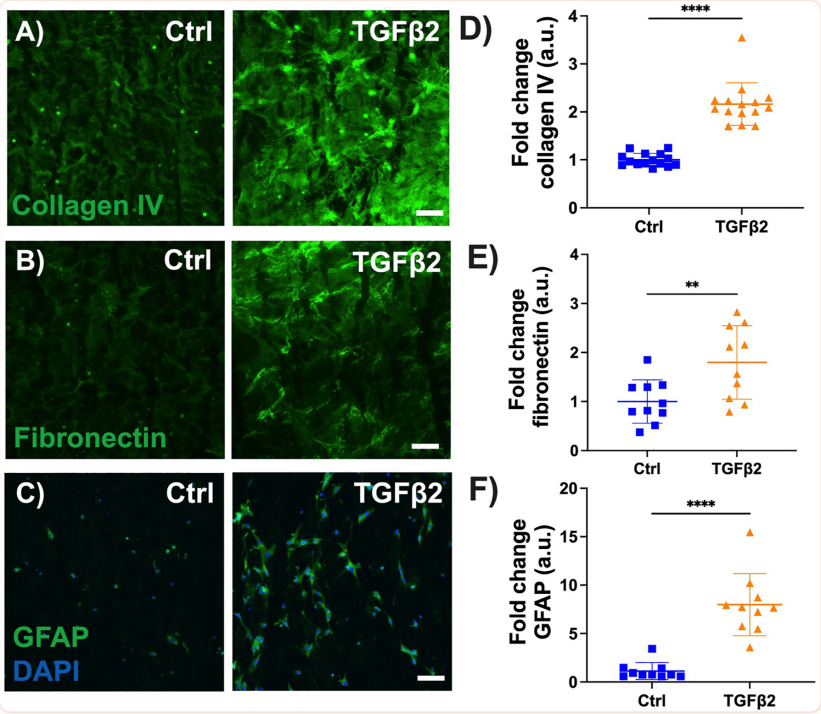

Fig. 6.

Effect of TGFβ2 on ECM protein and GFAP levels. (A–C) Representative fluorescence images of collagen IV, fibronectin, GFAP expression in control versus 5 ng/ml TGFβ2-treated MONHA-encapsulated hydrogels. Scale bar: 100 μm. (D–F) Quantification of fold change in signal intensity for collagen IV, fibronectin deposition, and GFAP expression shows significant difference between groups. (N = 5–7 fields of view/group for 2 strains). Statistical significance was determined using unpaired *t*-test (**p < 0.001, ****p < 0.0001).

4. Discussion

In glaucoma, elevated IOP progressively injures RGC axons within the ONH, leading to irreversible blindness. Evidence suggests that astrocytes residing within the unmyelinated ONH are one of the first responders to IOP elevation (Cooper et al., 2020; Hernandez, 2000; Sun et al., 2017; Wang et al., 2017b). Initially, astrocyte reactivity provides support to RGCs via increased gap junction coupling and nutrient transfer (Blanco-Suarez et al., 2017; Cooper et al., 2020; Sun et al., 2017). However, there is evidence that excessive reactivity can become neurotoxic later in the disease and adversely affect the health of RGC axons, partially by increasing ECM protein deposition and altering the astrocyte microenvironment (Clarke and Barres, 2013; Liddelow et al., 2017; Sterling et al., 2020). Given the relatively quick response time (hours – days) of ONH astrocytes to IOP elevation, a compelling hypothesis is that ONH astrocytes directly respond to IOP-induced mechanical strain to modulate nutrient transfer and ECM remodeling. In order to isolate cellular response to mechanical strain, *in vitro* cultures represent an ideal system to investigate mechanisms governing this response. Therefore, in this study, we sought to design a culture system that would allow for application of mechanical strains, and permit analyses of cell-cell and cell-ECM interactions.

While many investigations on astrocyte behavior include conventional cell culture model systems, there are several limitations to traditional 2D culture, namely supraphysiologic substrate stiffnesses and the lack of a 3D scaffold. These limitations can translate into a less faithful representation of *in vivo* astrocyte star-shaped morphology and function. Many cells are intrinsically sensitive to substrate stiffness. For example, mesenchymal stem cells seeded on stiff substrates (>10 kPa) and conventional tissue culture plastic dishes retain mechanical information and behave differently to cells cultured on substrates similar in stiffness to human tissue (<5 kPa) (Heo et al., 2015; Price et al., 2021; Yang et al., 2014). As such, newer *in vitro* models seek to incorporate these nuances to more reliably model astrocyte behavior. Some groups have used viscoelastic polymer hydrogels to better model the 3D architecture of neural tissues. Since collagen and HA are rich within neural tissues, a majority of 3D hydrogels consist of collagen, collagen/HA, or collagen/HA/matrigel combinations to promote quiescent astrocyte stellate morphology (Placone et al., 2015). However, when specifically studying ONHA behavior, important caveats to these methodologies include both the slow polymerization rate (i.e., 15–30 min required for collagen/HA gel formation at 37 °C) and the batch-to-batch variability of matrigel (Caliari and Burdick, 2016). These aspects may affect ONHA viability and produce differences in the biochemical and mechanical properties of hydrogels from one preparation to another and thus, impact cellular behavior differently each time.

In order to circumvent hydrogel inconsistencies associated with slow polymerization rate and batch-to-batch polymer variability, we used short duration UV-mediated crosslinking and well-defined ECM proteins for hydrogel construction. We recently published on a UV-crosslinked trabecular meshwork hydrogel system using Irgacure as a photoinitiator, which allows rapid (seconds to minutes) crosslinking between photoactive ECM biopolymers (e.g., methacrylate-conjugated collagen type I, thiol-conjugated HA) (Li et al., 2021), and we sought to adapt this hydrogel for MONHA encapsulation. We formulated the hydrogel using a collagen:HA ratio of 3:1 for both its broad applicability across different cell types (Aleman et al., 2021; Mazzocchi et al., 2018, 2019) and its recent association with reduced baseline cortical astrocyte reactivity (Placone et al., 2015). Incidentally, our initial studies using Irgacure yielded suboptimal MONHA viability, and thus, we incorporated the photoinitiator riboflavin (vitamin B2) within our system instead. Riboflavin is widely used for ocular collagen crosslinking for the treatment of keratectasia and can prevent excessive axial elongation in highly myopic eyes (Iseli et al., 2016; Wollensak et al., 2003). As a photoinitator, riboflavin may stabilize mechanical characteristics of collagen-based hydrogels while providing cytoprotective benefits (Ahearne and Coyle, 2016; Heo et al., 2016; Piluso et al., 2020). In our studies, use of 0.025% riboflavin and low UV intensity (10.3 mW/cm^2) in the blue light range (405–500 nm) allowed for high MONHA viability after crosslinking for 5 min. Encapsulated MONHAs continued to proliferate over four weeks in culture. Moreover, the stiffness of this ECM hydrogel was well within the range of *in vivo* neural tissues (Budday et al., 2015, 2017), in stark contrast to widely used 2D culture systems of supraphysiologic stiffness.

ONH astrocytes *in vivo* are stellate in morphology with extended and branched processes to promote coupling with neighboring astrocytes and RGC axons for neurotrophic support (Cooper et al., 2018; Oberheim et al., 2009; Sun et al., 2017). To investigate whether MOHNAs would develop such a stellate morphology within our hydrogel system, we measured cell process elongation and complexity over time using Sholl analysis. We confirmed that MONHAs encapsulated within hydro-

gels possess typical star-shape morphology with increased processes extension and complexity over 28 days in culture. Moreover, MONHAs cultured for this duration expressed CX43 in processes branching to neighboring astrocytes. These findings support the use of this 3D hydrogel system to study process remodeling, gap junction communication, and nutrient transfer between astrocytes in response to glaucomatous insult.

Astrocyte reactivity and gliosis is a complex process that is not easily defined. Astrocyte reactivity encompasses a spectrum of activated states that include both neuroprotective and neurotoxic phenotypes (Escartin et al., 2021; Liddelow et al., 2017). In general, astrocyte reactivity is characterized by morphologic changes such as enlargement of soma/cell shape and cytoskeletal remodeling with thicker protrusive processes, as well as functional changes that alter the cell's microenvironment (Escartin et al., 2021; Vecino et al., 2016). In glaucoma, ONH astrocyte reactivity is associated with intrinsic F-actin remodeling, increased ECM protein deposition and upregulation of GFAP (Hernandez, 2000). To determine whether MONHA reactivity could be reliably induced in our system, we treated MONHA-encapsulated hydrogels with TGFβ2, which is known to be upregulated in glaucoma (Kim et al., 2017; Pena et al., 1999; Wang et al., 2017a; Zode et al., 2011). We observed that TGFβ2-treated MONHAs developed increased F-actin signal intensity, elevated fibronectin, and collagen IV protein deposition, and increased intracellular GFAP levels consistent with our previous work in 2D culture (Kirschner et al., 2021). Of note, our goal of using TGFβ2 was to demonstrate that encapsulated MONHAs would display altered cytoskeletal and matrix protein changes similar to 2D culture, but with more reliable morphologic characteristics. Future studies aim to use this system to investigate cellular response to more nuanced insults, such as biomechanical strain. Importantly, our hydrogel system enables – for the first time – accurate analyses of astrocyte morphological changes and the interplay between the surrounding ECM and astrocyte behavior in a relevant 3D microenvironment.

In conclusion, we have engineered a biomimetic MONHA-encapsulated hydrogel system to investigate key morphological aspects of ONH astrocyte behavior in response to insult that cannot be easily assessed via 2D cell culture. We acknowledge that there are several limitations to this model system as compared to *in vivo* analyses of ONH astrocyte morphology and behavior in glaucoma. Firstly, the glial lamina of rodents is distinct from the primate lamina cribrosa (Morrison et al., 2011), and it is possible that rodent-derived ONH astrocytes behave differently from primate-derived ONH astrocytes. Given that the ONH has been identified as the initial site of RGC injury in rodent models of IOP elevation (Howell et al., 2007), we sought to initially encapsulate mouse ONH astrocytes in our hydrogel. As an advancement of this model, future studies will aim to encapsulate primate-derived ONH astrocytes. Secondly, the collagen matrix within our engineered hydrogels is largely disorganized, in strong contrast to the organized collagenous lamina cribrosa of primates (Ling et al., 2019). Thirdly, MOHNA-encapsulated hydrogels are devoid of several key factors (i.e., additional ONH glia, such as microglia and lamina cribrosa cells, vascular support, and RGC axons) that regulate ONH astrocyte response to IOP elevation. Incorporation of these elements in future engineered models of the ONH is an exciting prospect. An advantage of the 3D MONHA-encapsulated hydrogel described herein is the ability to isolate astrocyte response to biomechanical insults (i.e., IOP-related mechanical strain and matrix stiffening), which is not possible using *in vivo* systems. Compressive/tensile strains conferred by elevated IOP and age-associated stiffening are thought to contribute significantly to ONH astrocyte reactivity in glaucoma

(Grytz et al., 2012; Korneva et al., 2020; Sigal et al., 2007), but the mechanisms underlying this response are unknown. We recently described a role of mechanosensitive channel activation in TGFβ2-induced MONHA dysfunction in 2D culture (Kirschner et al., 2021). In future experiments, we aim to use this 3D culture system to study how mechanosensitive channel activity may modulate MONHA response to such biophysical stressors.

Supplementary Material

Supplementary Figures

Click here to view. (1.1M, pdf)

Funding

This project was supported in part by a National Institutes of Health grant K08EY031755 (to P.S.G), an American Glaucoma Society Young Clinician Scientist Award (to P.S.G.), a Syracuse University BioInspired Seed Grant (to S.H.), unrestricted grants to SUNY Upstate Medical University Department of Ophthalmology and Visual Sciences from Research to Prevent Blindness (RPB) and from Lions Region 20-Y1, and RPB Career Development Awards (to S.H. and P.S.G.).

Acknowledgments

We thank Dr. Alison Patteson at Syracuse University for rheometer access, Drs. Audrey M. Bernstein and Mariano S. Viapiano, and the Neuroscience Microscopy Core at Upstate Medical University for imaging support, and Mona El Gendi for assisting with cell characterization.

Footnotes

Declaration of competing interest

The authors report no conflicts of interest.

Appendix A. Supplementary data

Supplementary data to this article can be found online at https://doi.org/10.1016/j.exer.2022.109102.

Data and materials availability

All data needed to evaluate the conclusions in the paper are present in the paper and/or the Supplementary Materials. Additional data related to this paper may be requested from the authors.

References

1. Ahearne M, Coyle A, 2016. Application of UVA-riboflavin crosslinking to enhance the mechanical properties of extracellular matrix derived hydrogels. *J. Mech. Behav. Biomed. Mater* 54, 259–267. [PubMed] [Google Scholar]
2. Aleman J, Sivakumar H, DePalma T, Zhou Y, Mazzocchi A, Huntwork RC, Yoo KM, Banks S, Clark C, Maycock A, Leaks K, Enck K, Opara E, Gatenholm P, Welker M, Soker S, Herberg S, Criswell T, Skardal A, 2021. Engineering a Thixotropic and Biochemically Tunable Hyaluronan and Collagen Bioink for Biofabrication of Multiple Tissue Construct Types. *bioRxiv*, 458584, 2021.2009.2001. [Google Scholar]
3. Alexander GM, Farris S, Pirone JR, Zheng C, Colgin LL, Dudek SM, 2016. Social and novel contexts modify hippocampal CA2 representations of space. *Nat. Commun* 7, 10300. [PMC free article] [PubMed] [Google Scholar]
4. Blanco-Suarez E, Caldwell AL, Allen NJ, 2017. Role of astrocyte-synapse interactions in CNS disorders. *J. Physiol* 595, 1903–1916. [PMC free article] [PubMed] [Google Scholar]
5. Boazak EM, d'Humieres J, Schildmeyer L, Kim G-A, Pareek P, Takayama S, Ethier CR, 2019. Towards optic nerve head on a chip: a tool for understanding glaucomatous optic neuropathy. *Invest. Ophthalmol. Vis. Sci* 60, 6171–6171. [Google Scholar]
6. Budday S, Nay R, de Rooij R, Steinmann P, Wyrobek T, Ovaert TC, Kuhl E, 2015. Mechanical properties of gray and white matter brain tissue by indentation. *J. Mech. Behav. Biomed. Mater* 46, 318–330. [PMC free article] [PubMed] [Google Scholar]
7. Budday S, Sommer G, Haybaeck J, Steinmann P, Holzapfel GA, Kuhl E, 2017. Rheological characterization of human brain tissue. *Acta Biomater* 60, 315–329. [PubMed] [Google Scholar]
8. Butt AM, Colquhoun K, Tutton M, Berry M, 1994. Three-dimensional morphology of astrocytes and oligodendrocytes in the intact mouse optic nerve. *J. Neurocytol* 23, 469–485. [PubMed] [Google Scholar]
9. Caliari SR, Burdick JA, 2016. A practical guide to hydrogels for cell culture. *Nat. Methods* 13, 405–414. [PMC free article] [PubMed] [Google Scholar]
10. Choi HJ, Sun D, Jakobs TC, 2015. Isolation of intact astrocytes from the optic nerve head of adult mice. *Exp. Eye Res* 137, 103–110. [PMC free article] [PubMed] [Google Scholar]
11. Clarke LE, Barres BA, 2013. Emerging roles of astrocytes in neural circuit development. *Nat. Rev. Neurosci* 14, 311–321. [PMC free article] [PubMed] [Google Scholar]
12. Clarke LE, Liddelow SA, Chakraborty C, Munch AE, Heiman M, Barres BA, 2018. Normal aging induces A1-like astrocyte reactivity. *Proc. Natl. Acad. Sci. U. S. A* 115, E1896–E1905. [PMC free article] [PubMed] [Google Scholar]
13. Cooper ML, Collyer JW, Calkins DJ, 2018. Astrocyte remodeling without gliosis precedes optic nerve Axonopathy. *Acta Neuropathol. Commun* 6, 38. [PMC free article] [PubMed] [Google Scholar]

14. Cooper ML, Pasini S, Lambert WS, D'Alessandro KB, Yao V, Risner ML, Calkins DJ, 2020. Redistribution of metabolic resources through astrocyte networks mitigates neurodegenerative stress. *Proc. Natl. Acad. Sci. U. S. A* 117, 18810–18821. [PMC free article] [PubMed] [Google Scholar]

15. Crawford Downs J, Roberts MD, Sigal IA, 2011. Glaucomatous cupping of the lamina cribrosa: a review of the evidence for active progressive remodeling as a mechanism. *Exp. Eye Res* 93, 133–140. [PMC free article] [PubMed] [Google Scholar]

16. Escartin C, Galea E, Lakatos A, O'Callaghan JP, Petzold GC, Serrano-Pozo A, Steinhauser C, Volterra A, Carmignoto G, Agarwal A, Allen NJ, Araque A, Barbeito L, Barzilai A, Bergles DE, Bonvento G, Butt AM, Chen WT, Cohen-Salmon M, Cunningham C, Deneen B, De Strooper B, Diaz-Castro B, Farina C, Freeman M, Gallo V, Goldman JE, Goldman SA, Gotz M, Gutierrez A, Haydon PG, Heiland DH, Hol EM, Holt MG, Iino M, Kastanenka KV, Kettenmann H, Khakh BS, Koizumi S, Lee CJ, Liddelow SA, MacVicar BA, Magistretti P, Messing A, Mishra A, Molofsky AV, Murai KK, Norris CM, Okada S, Oliet SHR, Oliveira JF, Panatier A, Parpura V, Pekna M, Pekny M, Pellerin L, Perea G, Perez-Nievas BG, Pfrieger FW, Poskanzer KE, Quintana FJ, Ransohoff RM, Riquelme-Perez M, Robel S, Rose CR, Rothstein JD, Rouach N, Rowitch DH, Semyanov A, Sirko S, Sontheimer H, Swanson RA, Vitorica J, Wanner IB, Wood LB, Wu J, Zheng B, Zimmer ER, Zorec R, Sofroniew MV, Verkhratsky A, 2021. Reactive astrocyte nomenclature, definitions, and future directions. *Nat. Neurosci* 24, 312–325. [PMC free article] [PubMed] [Google Scholar]

17. Foltz J, Schildmeyer L, Han W, Brown D, García A, Ethier CR, 2021. Morphometric analysis of rat optic nerve head (ONH) astrocytes grown in a 3D cell culture system. *Invest. Ophthalmol. Vis. Sci* 62, 2374–2374. [Google Scholar]

18. Grytz R, Sigal IA, Ruberti JW, Meschke G, Downs JC, 2012. Lamina cribrosa thickening in early glaucoma predicted by a microstructure motivated growth and remodeling approach. *Mech. Mater* 44, 99–109. [PMC free article] [PubMed] [Google Scholar]

19. Heo J, Koh RH, Shim W, Kim HD, Yim HG, Hwang NS, 2016. Riboflavin-induced photo-crosslinking of collagen hydrogel and its application in meniscus tissue engineering. *Drug Deliv. Transl. Res* 6, 148–158. [PubMed] [Google Scholar]

20. Heo SJ, Thorpe SD, Driscoll TP, Duncan RL, Lee DA, Mauck RL, 2015. Biophysical regulation of chromatin architecture instills a mechanical memory in mesenchymal stem cells. *Sci. Rep* 5, 16895. [PMC free article] [PubMed] [Google Scholar]

21. Hernandez MR, 2000. The optic nerve head in glaucoma: role of astrocytes in tissue remodeling. *Prog. Retin. Eye Res* 19, 297–321. [PubMed] [Google Scholar]

22. Hernandez MR, Igoe F, Neufeld AH, 1986. Extracellular matrix of the human optic nerve head. *Am. J. Ophthalmol* 102, 139–148. [PubMed] [Google Scholar]

23. Hernandez MR, Igoe F, Neufeld AH, 1988. Cell culture of the human lamina cribrosa. *Invest. Ophthalmol. Vis. Sci* 29, 78–89. [PubMed] [Google Scholar]

24. Howell GR, Libby RT, Jakobs TC, Smith RS, Phalan FC, Barter JW, Barbay JM, Marchant JK, Mahesh N, Porciatti V, Whitmore AV, Masland RH, John SW, 2007. Axons of retinal ganglion cells are insulted in the optic nerve early in DBA/2J glaucoma. *J. Cell Biol* 179, 1523–1537. [PMC free article] [PubMed] [Google Scholar]

25. Hu Y, Huang G, Tian J, Qiu J, Jia Y, Feng D, Wei Z, Li S, Xu F, 2021. Matrix stiffness changes affect astrocyte phenotype in an in vitro injury model. *NPG Asia Mater* 13. [Google Scholar]

26. Iseli HP, Korber N, Koch C, Karl A, Penk A, Huster D, Reichenbach A, Wiedemann P, Francke M, 2016. Scleral cross-linking by riboflavin and blue light application in young rabbits: damage threshold and eye growth inhibition. *Graefes Arch. Clin. Exp. Ophthalmol* 254, 109–122. [PubMed] [Google Scholar]

27. Kim ML, Sung KR, Shin JA, Young Yoon J, Jang J, 2017. Statins reduce TGF-beta2-modulation of the extracellular matrix in cultured astrocytes of the human optic nerve head. *Exp. Eye Res* 164, 55–63. [PubMed] [Google Scholar]

28. Kimball E, Schaub J, Quillen S, Keuthan C, Pease ME, Korneva A, Quigley H, 2021. The role of aquaporin-4 in optic nerve head astrocytes in experimental glaucoma. *PLoS One* 16, e0244123. [PMC free article] [PubMed] [Google Scholar]

29. Kirschner A, Strat AN, Yablonski J, Yoo H, Bague T, Li H, Zhao J, Bollinger KE, Herberg S, Ganapathy PS, 2021. Mechanosensitive channel inhibition attenuates TGFbeta2-induced actin cytoskeletal remodeling and reactivity in mouse optic nerve head astrocytes. *Exp. Eye Res* 212, 108791. [PMC free article] [PubMed] [Google Scholar]

30. Korneva A, Cone-Kimball EC, Nguyen TD, Quigley HA, 2020. Regional mechanical strains in mouse astrocytic lamina and peripapillary sclera after chronic IOP elevation. *Invest. Ophthalmol. Vis. Sci* 61, 996–996. [Google Scholar]

31. Li H, Bague T, Kirschner A, Strat AN, Roberts H, Weisenthal RW, Patteson AE, Annabi N, Stamer WD, Ganapathy PS, Herberg S, 2021. A tissue-engineered human trabecular meshwork hydrogel for advanced glaucoma disease modeling. *Exp. Eye Res* 205, 108472. [PubMed] [Google Scholar]

32. Li H, Raghunathan V, Stamer WD, Ganapathy PS, Herberg S, 2022. Extracellular Matrix Stiffness and TGFbeta2 Regulate YAP/TAZ Activity in Human Trabecular Meshwork Cells. *Front Cell Dev Biol* 10, 844342. [PMC free article] [PubMed] [Google Scholar]

33. Liddelow SA, Guttenplan KA, Clarke LE, Bennett FC, Bohlen CJ, Schirmer L, Bennett ML, Munch AE, Chung WS, Peterson TC, Wilton DK, Frouin A, Napier BA, Panicker N, Kumar M, Buckwalter MS, Rowitch DH, Dawson VL, Dawson TM, Stevens B, Barres BA, 2017. Neurotoxic reactive astrocytes are induced by activated microglia. *Nature* 541, 481–487. [PMC free article] [PubMed] [Google Scholar]

34. Ling YTT, Shi R, Midgett DE, Jefferys JL, Quigley HA, Nguyen TD, 2019. Characterizing the collagen network structure and pressure-induced strains of the human lamina cribrosa. *Invest. Ophthalmol. Vis. Sci* 60, 2406–2422. [PMC free article] [PubMed] [Google Scholar]

35. Lodge T, Hiemenz PC, 2020. *Polymer Chemistry*, third ed. CRC Press, Taylor & Francis Group, Boca Raton. [Google Scholar]

36. Lye-Barthel M, Sun D, Jakobs TC, 2013. Morphology of astrocytes in a glaucomatous optic nerve. *Invest. Ophthalmol. Vis. Sci* 54, 909–917. [PMC free article] [PubMed] [Google Scholar]

37. Mazzocchi A, Devarasetty M, Herberg S, Petty WJ, Marini F, Miller L, Kucera G, Dukes DK, Ruiz J, Skardal A, Soker S, 2019. Pleural effusion aspirate for use in 3D lung cancer modeling and chemotherapy screening. *ACS Biomater. Sci. Eng* 5, 1937–1943. [PMC free article] [PubMed] [Google Scholar]

38. Mazzocchi A, Devarasetty M, Huntwork R, Soker S, Skardal A, 2018. Optimization of collagen type I-hyaluronan hybrid bioink for 3D bioprinted liver microenvironments. *Biofabrication* 11, 015003. [PMC free article] [PubMed] [Google Scholar]

39. Morrison JC, Cepurna Ying Guo WO, Johnson EC, 2011. Pathophysiology of human glaucomatous optic nerve damage: insights from rodent models of glaucoma. *Exp. Eye Res* 93, 156–164. [PMC free article] [PubMed] [Google Scholar]

40. Mulvihill JJE, Raykin J, Snider EJ, Schildmeyer LA, Zaman I, Platt MO, Kelly DJ, Ethier CR, 2018. Development of a platform for studying 3D astrocyte mechanobiology: compression of astrocytes in collagen gels. *Ann. Biomed. Eng* 46, 365–374. [PubMed] [Google Scholar]

41. Neumann C, Garreis F, Paulsen F, Hammer CM, Birke MT, Scholz M, 2014. Osteopontin is induced by TGF-beta2 and regulates metabolic cell activity in cultured human optic nerve head astrocytes. *PLoS One* 9, e92762. [PMC free article] [PubMed] [Google Scholar]

42. Oberheim NA, Takano T, Han X, He W, Lin JH, Wang F, Xu Q, Wyatt JD, Pilcher W, Ojemann JG, Ransom BR, Goldman SA, Nedergaard M, 2009. Uniquely hominid features of adult human astrocytes. *J. Neurosci* 29, 3276–3287. [PMC free article] [PubMed] [Google Scholar]

43. Pena JD, Taylor AW, Ricard CS, Vidal I, Hernandez MR, 1999. Transforming growth factor beta isoforms in human optic nerve heads. *Br. J. Ophthalmol* 83, 209–218. [PMC free article] [PubMed] [Google Scholar]

44. Piluso S, Flores Gomez D, Dokter I, Moreira Texeira L, Li Y, Leijten J, van Weeren R, Vermonden T, Karperien M, Malda J, 2020. Rapid and cytocompatible cell-laden silk hydrogel formation via riboflavin-mediated crosslinking. *J. Mater. Chem. B* 8, 9566–9575. [PubMed] [Google Scholar]

45. Placone AL, McGuiggan PM, Bergles DE, Guerrero-Cazares H, Quinones-Hinojosa A, Searson PC, 2015. Human astrocytes develop physiological morphology and remain quiescent in a novel 3D matrix. *Biomaterials* 42, 134–143. [PMC free article] [PubMed] [Google Scholar]

46. Prendes MA, Harris A, Wirostko BM, Gerber AL, Siesky B, 2013. The role of transforming growth factor beta in glaucoma and the therapeutic implications. *Br. J. Ophthalmol* 97, 680–686. [PubMed] [Google Scholar]

47. Price CC, Mathur J, Boerckel JD, Pathak A, Shenoy VB, 2021. Dynamic self-reinforcement of gene expression determines acquisition of cellular mechanical memory. *Biophys. J* 120, 5074–5089. [PMC free article] [PubMed] [Google Scholar]

48. Ricard CS, Kobayashi S, Pena JD, Salvador-Silva M, Agapova O, Hernandez MR, 2000. Selective expression of neural cell adhesion molecule (NCAM)-180 in optic nerve head astrocytes exposed to elevated hydrostatic pressure in vitro. *Brain Res. Mol. Brain Res* 81, 62–79. [PubMed] [Google Scholar]

49. Schmittgen TD, Livak KJ, 2008. Analyzing real-time PCR data by the comparative C (T) method. *Nat. Protoc* 3, 1101–1108. [PubMed] [Google Scholar]

50. Sigal IA, Flanagan JG, Tertinegg I, Ethier CR, 2007. Predicted extension, compression and shearing of optic nerve head tissues. *Exp. Eye Res* 85, 312–322. [PubMed] [Google Scholar]

51. Sloan SA, Barres BA, 2014. Mechanisms of astrocyte development and their contributions to neurodevelopmental disorders. *Curr. Opin. Neurobiol* 27, 75–81. [PMC free article] [PubMed] [Google Scholar]

52. Stein JD, Khawaja AP, Weizer JS, 2021. Glaucoma in adults-screening, diagnosis, and management: a review. *JAMA* 325, 164–174. [PubMed] [Google Scholar]

53. Sterling JK, Adetunji MO, Guttha S, Bargoud AR, Uyhazi KE, Ross AG, Dunaief JL, Cui QN, 2020. GLP-1 receptor agonist NLY01 reduces retinal inflammation and neuron death secondary to ocular hypertension. *Cell Rep* 33, 108271. [PMC free article] [PubMed] [Google Scholar]

54. Sun D, Lye-Barthel M, Masland RH, Jakobs TC, 2009. The morphology and spatial arrangement of astrocytes in the optic nerve head of the mouse. *J. Comp. Neurol* 516, 1–19. [PMC free article] [PubMed] [Google Scholar]

55. Sun D, Moore S, Jakobs TC, 2017. Optic nerve astrocyte reactivity protects function in experimental glaucoma and other nerve injuries. *J. Exp. Med* 214, 1411–1430. [PMC free article] [PubMed] [Google Scholar]

56. Tehrani S, Davis L, Cepurna WO, Choe TE, Lozano DC, Monfared A, Cooper L, Cheng J, Johnson EC, Morrison JC, 2016. Astrocyte structural and molecular response to elevated intraocular pressure occurs rapidly and precedes axonal tubulin rearrangement within the optic nerve head in a rat model. *PLoS One* 11, e0167364. [PMC free article] [PubMed] [Google Scholar]

57. Tehrani S, Davis L, Cepurna WO, Delf RK, Lozano DC, Choe TE, Johnson EC, Morrison JC, 2019. Optic nerve head astrocytes display axon-dependent and -independent reactivity in response to acutely elevated intraocular pressure. *Invest. Ophthalmol. Vis. Sci* 60, 312–321. [PMC free article] [PubMed] [Google Scholar]

58. Vecino E, Rodriguez FD, Ruzafa N, Pereiro X, Sharma SC, 2016. Glia-neuron interactions in the mammalian retina. *Prog. Retin. Eye Res* 51, 1–40. [PubMed] [Google Scholar]

59. Wang J, Harris A, Prendes MA, Alshawa L, Gross JC, Wentz SM, Rao AB, Kim NJ, Synder A, Siesky B, 2017a. Targeting transforming growth factor-beta signaling in primary open-angle glaucoma. *J. Glaucoma* 26, 390–395. [PubMed] [Google Scholar]

60. Wang R, Seifert P, Jakobs TC, 2017b. Astrocytes in the optic nerve head of glaucomatous mice display a characteristic reactive phenotype. *Invest. Ophthalmol. Vis. Sci* 58, 924–932. [PMC free article] [PubMed] [Google Scholar]

61. Weinreb RN, Aung T, Medeiros FA, 2014. The pathophysiology and treatment of glaucoma: a review. *JAMA* 311, 1901–1911. [PMC free article] [PubMed] [Google Scholar]

62. Wollensak G, Spoerl E, Seiler T, 2003. Riboflavin/ultraviolet-a-induced collagen crosslinking for the treatment of keratoconus. *Am. J. Ophthalmol* 135, 620–627. [PubMed] [Google Scholar]

63. Yang C, Tibbitt MW, Basta L, Anseth KS, 2014. Mechanical memory and dosing influence stem cell fate. *Nat. Mater* 13, 645–652. [PMC free article] [PubMed] [Google Scholar]

64. Zode GS, Sethi A, Brun-Zinkernagel AM, Chang IF, Clark AF, Wordinger RJ, 2011. Transforming growth factor-beta2 increases extracellular matrix proteins in optic nerve head cells via activation of the Smad signaling pathway. *Mol. Vis* 17, 1745–1758. [PMC free article] [PubMed] [Google Scholar]